Spatiotemporal Dynamics of Covert Attention With Different Degrees of Central Visual Field Defects: An ERP and sLORETA Study

Chaoqun Shi, Sinan Liu, Bingyang Zhao, Yu Meng, Xin Gong, Xiping Chen, and Luyang Tao

Department of Forensic Medicine, School of Basic Medicine and Biological Sciences, Affiliated Guangji Hospital, Soochow University, Suzhou, China

Correspondence: Xiping Chen and Luyang Tao, 178 Ganjiang East Road, Suzhou, China; xipingchen@suda.edu.cn; taoluyang@suda.edu.cn.

CS and SL contributed equally to this work.

Received: January 10, 2022
Accepted: April 10, 2022
Published: April 26, 2022

Citation: Shi C, Liu S, Zhao B, et al. Spatiotemporal dynamics of covert attention with different degrees of central visual field defects: An ERP and sLORETA study. *Invest Ophthalmol Vis Sci.* 2022;63(4):19. https://doi.org/10.1167/iovs.63.4.19

Purpose. The present study aimed to investigate the spatiotemporal dynamics of covert attention by simulating different degrees of central visual field defects in healthy subjects.

Methods. An electroencephalogram (EEG) was recorded while 40 normal-sighted subjects performed a target discrimination task. Target stimuli simulated different defect degrees of the central visual field by artificially central scotomas (5, 10, 20, and 30 degrees of visual angle) masked on the center of black-and-white checkerboards. Event-related potentials (ERPs) and standardized low-resolution brain electromagnetic tomography (sLORETA) based on ERPs were analyzed.

Results. ERP results indicated that during early perceptual processes, compared with 5-degree and 10-degree defects, N1 amplitudes of 20-degree and 30-degree defects decreased, whereas P2 amplitudes significantly reduced in 30-degree defects. During later discrimination and decision processing, N2 amplitudes gradually increased from 5-degree to 30-degree defects, whereas P3 amplitudes gradually decreased. Source localization indicated that 5-degree and 10-degree defects had stronger activations than 20-degree and 30-degree defects from the occipital cortex to the ventral stream and dorsal streams. Especially, 30-degree defects primarily recruited additional activations in the ventrolateral prefrontal cortex and ventral stream and later caused the disconnection of dorsolateral prefrontal-posterior parietal cortices in the dorsal stream.

Conclusions. Different degrees of central visual field defects differed in distinct spatiotemporal characteristics at multiple stages of covert attention, from top-down forward feedback and attentional allocation to executive controls through ventral and dorsal processing streams, suggesting that the combination of ERP and source localization can reveal the spatiotemporal control capacity of the cortex on central visual field defects.

Keywords: covert attention, central visual field defects (CVFDs), event-related potentials (ERPs), standardized low-resolution brain electromagnetic tomography analysis (sLORETA), dorsal stream, ventral stream

Covert attention is a fundamental aspect of perception and cognition that allows us to selectively process and prioritize incoming visual information at a given location in the visual field without directing gaze.[1,2] Extensive literature suggests that covert attention is not uniform throughout the visual field.[3,4] Using a paradigm with inhibition of return, some studies suggest that the inhibitory control of covert attention is stronger at the periphery (21 degrees of eccentricity) than at the perifoveal visual field (7 degrees).[5,6] Other studies suggest that compared with foveal targets (1 degree), targets in the perifoveal visual field showed greater exogenous inhibition and endogenous facilitation.[7,8] These findings suggest that the attentional modulation in the visual field depends on stimulus locations in the visual field. However, to our knowledge, little is known about the effects of visual field defects on the deployment of covert attention.

In daily life, patients with central visual field defects decline worse in quality of life compared with those with peripheral visual field defects. Given that retinotopy is the basic principle of visual cortex organization,[9] flexible manipulation of spatial location is an effective tool for studying the visual field. Considering the highly individual differences in the patient population,[10,11] we utilized artificial scotomas to simulate visual field defects in visually healthy participants. Artificial scotoma provides a practical alternative to simulate a certain retinal lesion by superimposing a visual mask on a stimulus background.[12] Some studies have used a central blank field surrounded by a high-contrast checkerboard stimulus to simulate central visual field defects and found the amplitudes of visual evoked potential (VEP) progressively decreased as the diameter of central defects increased.[13] Others found the early P1 component of extrastriate generators increased in amplitude in a simulated retinal scotoma relative to healthy controls.[14] Because VEPs can only quantify functional integrity in the retina and early afferent visual pathways,[15] the temporal course of such visual field defects,

whether they affect early, lower-level visual processing, or somewhat later, higher-order cognitive processing, is still not fully understood.

Event-related potentials (ERPs) provide high-resolution measures for the time course of neural activity associated with specific aspects of perceptual and/or cognitive processing. Stimuli at attended locations elicit enlarged early exogenous P1 or N1 components or both over the posterior scalp regions. This is interpreted as the sensory gain control mechanism, which increases the acuity of visual perception at attended locations and propagated to each subsequent stage of processing.[16] The P1 comes from the dorsal extrastriate cortex and is sensitive to low-level stimulus properties, such as spatial frequency, contrast, and luminance, whereas the N1 is more pronounced for high-load stimuli relative to low-load stimuli and reflects a general discrimination process influenced by spatial attention.[17,18] The posterior P2 amplitudes increase for stimuli appearing at the periphery and might be a sign of reactivation in the extrastriate cortex, due to top-down feedback from higher visual areas back to the primary visual cortex.[19] Late cognitive processes are reflected by late endogenous ERP components (N2 and P3). The N2 is modulated by the probability of task-relevant stimulus categories and reflects the ability to discriminate an incongruity between the input stimulus and the stimulus representation stored in memory,[20] and the P3 is a reliable indicator reflecting the high-level cognitive processing resources, such as attentional allocation and contextual updating of working memory.[21] Taken together, ERPs reveal multiple stages of distinct perceptual and cognitive processes initiated by the attention process.

Considering that ERP analysis does not directly indicate the active location of the neural source in the cerebral cortex, source localization analysis (e.g. standardized low-resolution electromagnetic tomography analysis [sLORETA])[22] can be used to dynamically reveal widespread activation of multiple regions during attentional deployment. Cortical activation after visual stimulation is initially in the visual occipital cortex, processing information input from the attended spatial location.[23,24] Then, visual processing splits into two parallel cortical streams and performs distinct visual functions based on stimulus attributes: the dorsal stream follows a route from the occipital cortex to the posterior parietal cortex, whereas the ventral stream forms a pathway connecting the occipital cortex with the inferior temporal gyrus. The dorsal streams are dedicated to the control of visually guided behaviors, whereas the ventral streams are linked to the conscious perception of visual representations.[25] The prefrontal cortex involves top-down control of sensory signals within posterior cortices, such as anticipation, judgment, planning, and decision making, known as the executive control network.[26] It is well known that visual attention involves extensive cortical activation, but when visual attention is altered due to removal of the visual stimulus, how do the associated visual cortical areas respond? There have been few studies on cortical activation in visual field defects until now.

Here, combined with ERP and source localization analysis, we aimed to explore spatiotemporal dynamics of attentional deployment when normal-sighted individuals simulated central visual field defects. Black-and-white checkerboard stimuli are available to activate both the striate and extrastriate cortex[27] and thus serve as visual stimulation throughout the task. Target stimuli simulated central visual field defects using artificial central scotoma, masking the black disks on the center of the full-field checkerboards to deprive visual inputs of the central retina. By independently varying the diameter of black disks from 5, 10, and 20 to 30 degrees of visual angle, we manipulated 4 central visual field defect conditions. We hypothesized that simulated visual field defects caused impaired information inputs during target discrimination tasks, resulting in the differential attentional deployment of sensory-perceptual processes (P1, N1, and P2) and cognitive processing (N2 and P3) and neural activation in an extensive network of brain regions. As the diameter of the central scotoma increased, the attentional allocation to visual inputs decreased, and the difficulty in capturing peripheral visual stimulation increased correspondently. We predicted that as defect degrees of the central visual field increased, the amplitude of positive ERP components gradually decreased, and the amplitude of negative ERP components gradually increased. Source activations characterized by top-down processing can also differentiate defect degrees of the central visual field in the strength of source activation. To summarize, we considered that the combination of ERP and source localization could be used as the more effective electrophysiological measures to objectively detect and evaluate the spatiotemporal capacity in central visual field defects.

Materials and Methods

Participants

Forty subjects (24 men, mean age = 23.4 ± 3.5 years) from Soochow University participated in the experiment. All participants were right-handed and had normal or corrected-to-normal vision and no history of mental or neurological disorders. All participants were recruited as volunteers and gave informed written consent before the experiment. The experiment was approved by the ethical committee of Soochow University in compliance with the Declaration of Helsinki.

Stimuli

A visual three-stimulus oddball paradigm was used, which presents an infrequent target stimulus in a background of frequently occurring standard stimuli and infrequently occurring distracter stimuli (see Fig. 1).[28] The standard stimuli were the full-field black-and-white checkerboard pattern. The checkerboard stimuli had a mean luminance of 50 cd/m^2 and a Michelson contrast between black and white squares of 96%. The size of a single check subtended 32 inches of visual angle per side. The target stimuli were black disks masked in the center of black-and-white checkerboards. The black disks had a constant luminance of 0 cd/m^2. The setup of target stimuli simulated the acute negative effect of a central scotoma by using the same black color for the central disk and background. The diameter of black disks varied from 5, 10, and 20 to 30 degrees of visual angle. The distractor stimuli were black-and-white checkerboard disks masked in the center of the black background. The size of the black-and-white checkerboards maintained a constant diameter of 10 degrees. The setup of distractor stimuli disturbed attention and increased the difficulty of discriminating target stimuli by reversing stimulus patterns. A red cross of 1 degree was placed in the center of the monitor, and participants were instructed to fixate this cross throughout visual stimulation. The whole experiment consisted of four defect conditions, and each condition included four blocks (4 conditions × 4 blocks). Each block contained 200 trials of 140 standard

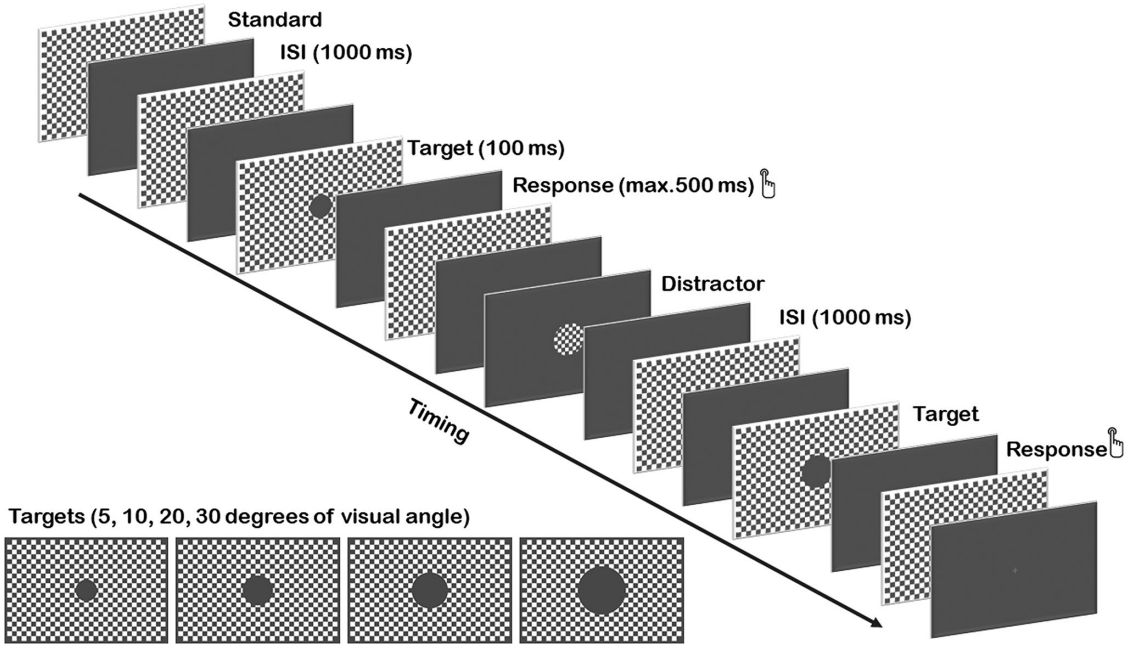

Figure 1. Overview of a visual three-stimulus oddball paradigm with the stimulus categories and trial sequences. The visual three-stimulus oddball paradigm consisted of standard stimuli (70%), target stimuli (15%), and distractor stimuli (15%). All stimuli were presented in a pseudorandom sequence. Standard stimuli were black-and-white checkerboards. Target stimuli were different diameters of black disks masked on the center of the checkerboards (5, 10, 20, and 30 degrees of visual angle). Distractor stimuli were circular checkerboards of the constant 10 degrees superimposed on the black backgrounds. Participants were instructed to press the "N" button with the right hand for target stimuli, to press the "V" button with the left hand for distractor stimuli, and not respond to standard stimuli.

stimuli (probability = 70%), 30 target stimuli (probability = 15%), and 30 distractor stimuli (probability = 15%). The presentation order of four defect conditions was counterbalanced in a pseudorandom way. Using E-prime software, all stimuli were presented on a 17-inch computer monitor with a framerate of 60 Hz and a resolution of 1024 × 768 pixels. The stimulus presentation time was 100 ms, and the interstimulus interval was set at 1000 ms, including a 500 ms response window. To ensure the effectiveness of the oddball paradigm and avoid habituation and anticipation, the order of stimuli was presented in a pseudorandom sequence. There were at least two standards between two targets or distractors, and any two target or distractor stimuli could not be displayed continuously. Before formal blocks, participants completed one block to get familiar with the experiment.

Procedure

The experiment was conducted in a dimly lit, sound-attenuated, and electrically shielded room. To avoid getting closer change of the visual angle and keep the replicability and the validity of the experiment, the participants were required to sit in a comfortable chair at a 40 cm distance from the computer monitor, with the chin-rest to aid in head stabilization. The chair height was adjusted to ensure that the height of the participant's test eye was in line with the center of the computer monitor. Participants were asked to randomly cover one eye with a black patch and tested monocularly. The test eye was counterbalanced across participants. Each participant was instructed to maintain fixation at the central cross of the screen during an experimental trial. To eliminate or reduce the interference of the background environment, electroencephalogram (EEG) recording was carried out in a dark room and the frame of the computer monitor was also covered by black cardboard.

Each participant was instructed to press the button on the keyboard alternately with both hands, pressing the "N" button with the right hand for target stimuli, and pressing the "V" button with the left hand for distractor stimuli, and there was no need to respond to standard stimuli. In the experiment, the buttons pressed by the right and left hands were counterbalanced across target stimuli and distractor stimuli to mitigate the impact of the motor cortex. For missing (absence of button presses after target stimuli) and false alarms (button presses after standard or distractor stimuli), the corresponding responses were excluded from the analysis. Mean reaction time (RT) and accuracy (ACC) for target stimuli were calculated for each participant. Because our setup of distractor stimuli was to improve the difficulty of target identification, the distractor stimuli were not analyzed in the subsequent experiment.

EEG Recording and ERP Analysis

Continuous EEGs were recorded using a NeuroScan Synamps[2] Amplifier system. The 32-channel active Ag/AgCl scalp electrodes were mounted according to the international 10-10 system and referenced online to the average of left and right mastoids, with a ground electrode at the FPZ. To monitor blinks and eye movements, horizontal electrooculograms (EOGs) were recorded from bipolar electrodes placed on the left and right canthi, and vertical EOGs were recorded from bipolar electrodes placed above and below the left eye. EEG and EOG data were filtered with a bandpass of approximately 0.1 to 100 Hz and digitally sampled at 1000 Hz. The impedance of all electrodes was maintained below 5 kΩ.

All EEG data were processed and analyzed using the EEGLAB and Letswave Toolbox in MATLAB (The MathWorks Inc. R2019b).[29] Raw EEG data were first digitally filtered using a Butterworth Zero Phase filter (approximately 0.05 to 30 Hz, 24 dB/oct slope). Components related to eye blinks, eye movements, and other artifacts were rejected based on visual inspection using an independent component analysis (ICA) algorithm.[30] Continuous EEG data were then segmented into epochs of 1000 ms (200 ms pre-stimulus to 800 ms post-stimulus), including a pre-stimulus 200 ms used for baseline correction. Epochs were re-referenced to an average reference. Single epochs containing muscle activity or amplifier blocking were rejected offline before averaging, and the rejection criterion was ± 100 µV. After artifact rejection, at least 85% of the epochs per condition per subject were included in the analysis, and there were no large differences across conditions. Grand-averaged ERP waveforms were computed for target stimuli in each visual field defect condition.

To minimize researcher degrees of freedom, measuring parameters (i.e. time windows and electrodes) were based on previous ERP studies[31,32] and visual inspection of the grand-averaged ERP waveforms and brain topographic maps, which were performed using a collapsed localizer.[33] We calculated the largest voltages for each component first, collapsed across all conditions to create a grand average waveform, and then selected the time windows and electrodes where overall activity was greatest. Therefore, the time windows of interest were defined as follows: P1 = approximately 70 to 110 ms; N1 = approximately 110 to 170 ms; P2 = approximately 170 to 230 ms; N2 = approximately 230 to 270 ms; and P3 = approximately 300 to 500 ms. Regions of interest (ROIs) electrodes were chosen as follows: the occipital regions (O1/Z/2) for the P1 and P2 components, the parietal regions (P3/Z/4) for the N1 component, and the central-parietal and parietal regions (CP3/Z/4 and P3/Z/4) for the N2 and P3 components.

Source Localization Analysis

In a subsequent analysis, the sLORETA software was used to reveal the differences between experimental conditions for each ERP component. The sLORETA algorithm solves the inverse problem by assuming related orientations and strengths of neighboring neuronal sources.[34] Source localization computations are based on a realistic head model registered to the Talairach human brain atlas,[35] available as digitized magnetic resonance imaging (MRI) at the Montreal Neurologic Institute (MNI).[36] The solution space is restricted to the cortical gray matter and the hippocampus, producing a total of 6239 voxels at 5 mm spatial resolution. Recent studies have shown that the localization error distance of sLORETA based on 32-channel configurations is approximately 1.45 to 3.38 mm,[37] which is lower than the 5 mm spatial resolution in our analysis. When using at least 25 scalp electrodes, the sLORETA solutions showed significant correspondence with those provided by hemodynamic procedures.[38,39] Numerous sLORETA studies have shown that the sLORETA software based on 32-channel configurations is an effective tool for locating neural activity.[40,41]

For each participant and condition, the sLORETA images were calculated for the scalp-recorded activity for each ERP component in the selected time window (mean latency ± SD). Based on previously published studies of visual attention,[42,43] we performed an ROI analysis on four cortical ROIs to investigate possible source differences among defect conditions (prefrontal regions, temporal regions, parietal regions, and occipital regions). The log-transformed standardized current density values for each ROI were computed for each participant and condition and statistically compared using SPSS. All source estimation procedures were performed using open the sLORETA software (http://www.uzh.ch/keyinst/loretaOldy.htm).

Statistical Analysis

Statistical analyses were conducted using IBM SPSS Statistics, version 20.0.

Behavioral data (RTs and ACC) were analyzed by 1-way analysis of variance (ANOVA) with the defect condition (4 levels: 5 vs. 10 vs. 20 vs. 30 degrees) as the within-subject factor.

For ERP components, the mean amplitudes and peak latencies were analyzed by the repeated-measures ANOVA. P1, N1, and P2 were analyzed with the defect condition (4 levels: 5 vs. 10 vs. 20 vs. 30 degrees) and laterality (3 levels: left vs. middle vs. right) as the within-subject factors. N2 and P3 were analyzed with the defect condition (4 levels: 5 vs. 10 vs. 20 vs. 30 degrees), ROI (2 levels: the central-parietal and parietal regions), and laterality (3 levels: left vs. middle vs. right) as the within-subject factors.

For source localization, the log-transformed standardized current density was analyzed by repeated-measures ANOVA with the defect condition (4 levels: 5 vs. 10 vs. 20 vs. 30 degrees) as the within-subject factor.

The main and interaction effects were reported first, followed by post hoc analyses. As measures of effect size, partial eta squared ($\eta 2$) was reported for ANOVAs. The Greenhouse-Geisser correction was applied in all analyses when appropriate. All the comparison P levels reported below were subjected to Bonferroni correction. For all statistical tests, the significance level was set to $\alpha = 0.05$, bilaterally (2-tailed). Post hoc power analysis for ANOVA using G*Power version 3.1.9.7. was performed to evaluate whether the results had sufficient verification power.[44] Only the results with statistical power over sufficient limits (80%) were statistically effective.[45] The relevant statistical power and effect sizes of the results are listed in Supplementary Table S1.

Correlation Analysis

For significant source activations, the Pearson correlation coefficient analyses were used to disclose the relationship between different source activations to illustrate information flows of visual processing. This correlation method was used based on the detection of the data as a normal distribution.

Results

Behavioral Results

Mean RTs showed significant main effects of the defect condition ($F(3, 117) = 6.885$, $P < 0.001$, partial $\eta^2 = 0.150$), indicating that the RTs of 5-degree and 10-degree defects were smaller than that of 30-degree defects (5-degree = 366.7 ms < 30-degree: 389.1 ms, $P = 0.001$; and 10-degree = 372.3 ms < 30-degree: 389.1 ms, $P = 0.018$). ACCs also showed significant main effects of the defect condition ($F(3,117) = 7.109$, $P < 0.001$, partial $\eta^2 = 0.154$), indicat-

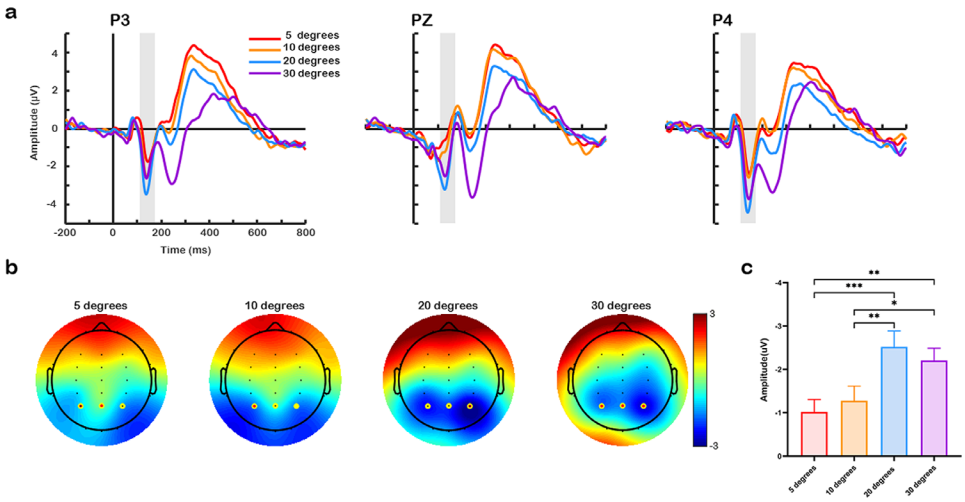

Figure 2. ERP results for target N1 component. (**a**) Grand average ERP waveforms for target N1 component at parietal (P3-PZ-P4) electrode sites in microvolts (μV; *red*, *orange*, *blue*, and *purple lines* indicate 5, 10, 20, and 30-degree defect conditions, respectively). The *gray shaded areas* represent the time windows in which significant effects are found (approximately 110 to 170 ms). (**b**) Topographic scalp distributions of four central visual field defects corresponding to the target N1 time window (approximately 110 to 170 ms, in μV units). (**c**) Statistical results of target N1 amplitudes for each defect condition (*red*, *orange*, *blue*, and *purple bars* indicate the 5, 10, 20, and 30-degree defect conditions, respectively).

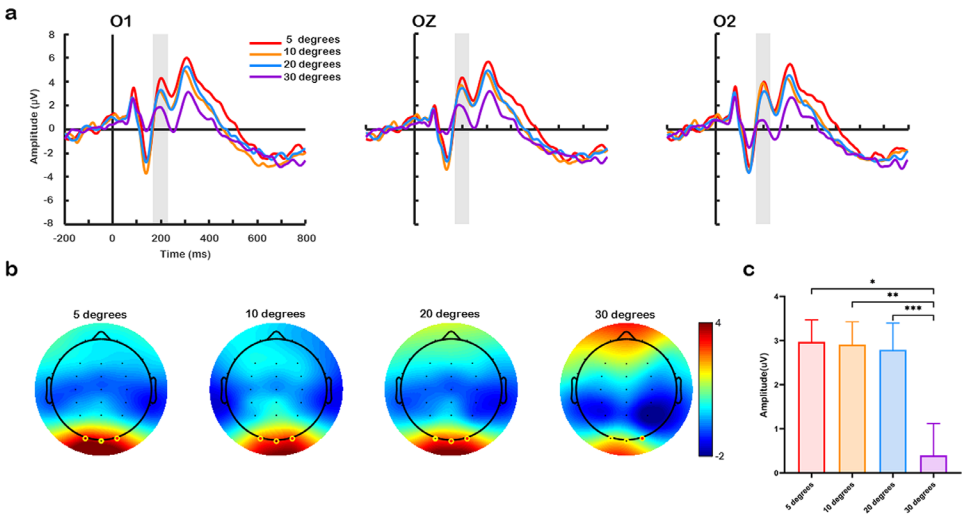

Figure 3. ERP results for target P2 component. (**a**) Grand average ERP waveforms for target P2 component at occipital (O1-OZ-O2) electrode sites in microvolts (μV; *red*, *orange*, *blue*, and *purple lines* indicate the 5, 10, 20, and 30-degree defect conditions, respectively). The *gray shaded areas* represent the time windows in which significant effects are found (approximately 170 to 230 ms). (**b**) Topographic scalp distributions of four central visual field defects corresponding to the target P2 time window (approximately 170 to 230 ms, in μV units). (**c**) Statistical results of target P2 amplitudes for each defect condition (*red*, *orange*, *blue*, and *purple bars* indicate the 5, 10, 20, and 30-degree defect conditions, respectively).

ing that the ACCs of 5-degree and 10-degree defects were larger than those of 30-degree defects (5-degree = 82.5% > 30-degree: 74.6%, $P < 0.001$; and 10-degree = 81.9% > 30-degree: 74.6%, $P = 0.008$).

ERP Results

For the mean amplitude of target ERPs, there were significant differences for the target N1, P2, N2, and P3 components between the different visual field defects, whereas for the peak latency of target ERPs, only the target P3 component had a significant difference between different visual field defects.

Target N1. Figure 2 shows the grand average waveforms (see Fig. 2a), topographic maps (see Fig. 2b), and the histograms of mean amplitudes (see Fig. 2c) for the target N1 component. There was a significant main effect of the defect condition ($F(3, 117) = 9.458$, $P < 0.001$, partial $\eta^2 = 0.195$) and laterality ($F(2, 78) = 10.418$, $P < 0.001$, partial $\eta^2 = 0.211$). For the main effect of the defect condition, pairwise comparisons showed that N1 amplitudes of 20-degree and 30-degree defects were larger (more negative) than those of

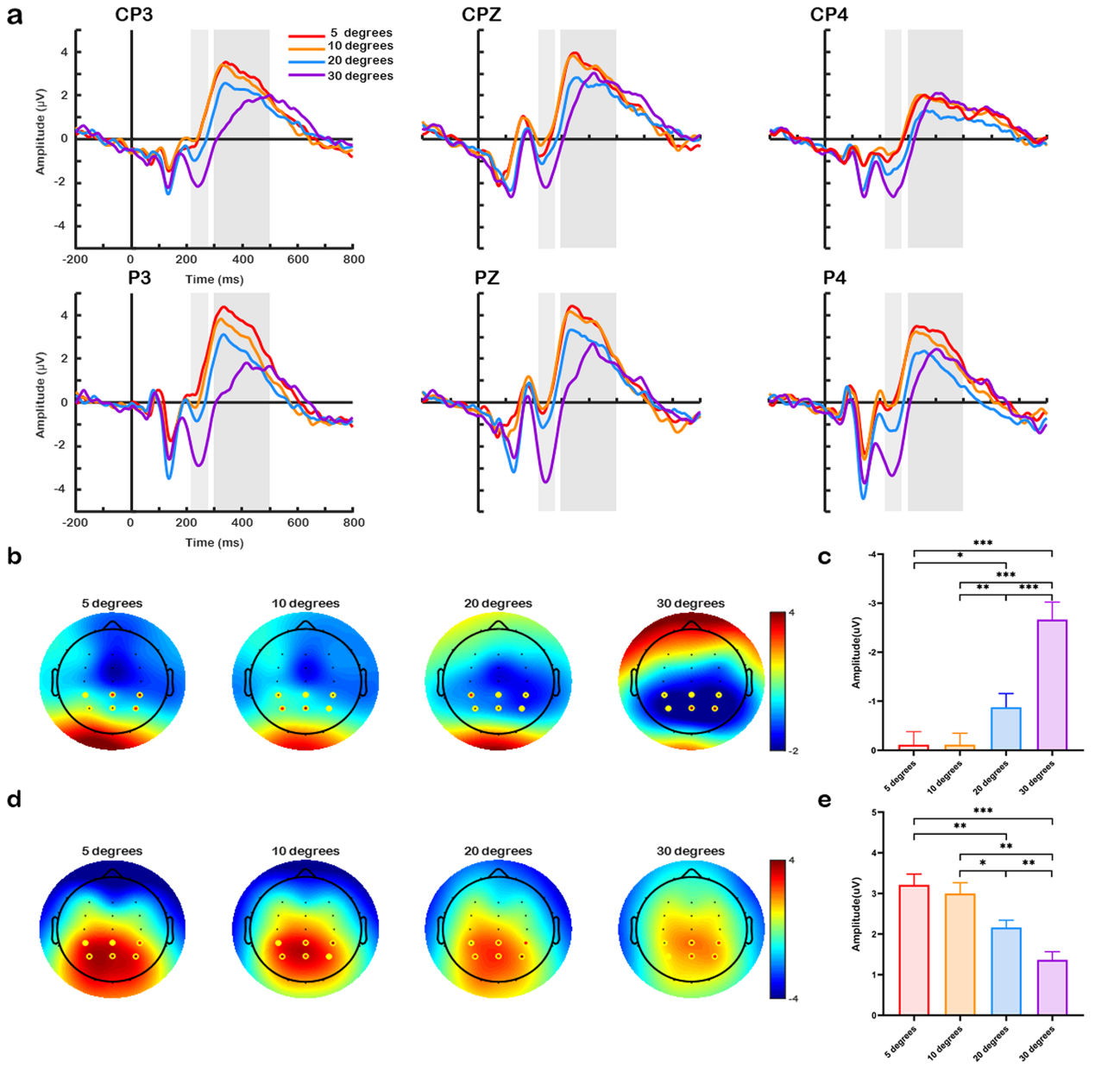

Figure 4. ERP results for target N2 and P3 components. (**a**) Grand average ERP waveforms for target N2 and P3 components at central-parietal and parietal (CP3-CPZ-CP4-P3-PZ-P4) electrode sites in microvolts (μV; *red*, *orange*, *blue*, and *purple lines* indicate the 5, 10, 20, and 30-degree defect conditions, respectively). The *gray shaded areas* represent the time windows in which significant effects were found (approximately 230 to 270 ms for the target N2 and approximately 300 to 450 ms for the target P3). (**b**) Topographic scalp distributions of four central visual field defects corresponding to the target N2 time window (approximately 230 to 270 ms, in μV units). (**c**) Statistical results of target N2 amplitudes for each defect condition (*red*, *orange*, *blue*, and *purple bars* indicate the 5, 10, 20, and 30-degree defect conditions, respectively). (**d**) Topographic scalp distributions of four central visual field defects corresponding to the target P3 time window (approximately 300 to 450 ms, in μV units). (**e**) Statistical results of target P3 amplitudes for each defect condition (*red*, *orange*, *blue*, and *purple bars* indicate the 5, 10, 20, and 30-degree defect conditions, respectively).

the 5-degree and 10-degree defects (5-degree < 20-degree, $P < 0.001$; 5-degree < 30-degree, $P = 0.005$; 10-degree < 20-degree, $P = 0.006$; and 10-degree < 30-degree, $P = 0.028$). For the main effect of laterality, N1 amplitudes in the right hemispheres were larger (more negative) than those in the middle regions (middle < right, $P < 0.001$).

Target P2. Figure 3 shows the grand average waveforms (see Fig. 3a), topographic maps (see Fig. 3b), and the histograms of mean amplitudes (see Fig. 3c) for the target P2 component. There was a significant main effect of the defect condition (F (3, 117) = 7.689, $P = 0.001$, partial $\eta^2 = 0.165$), indicating that P2 amplitudes of 30-degree defects were smaller than those of the other defects (30-degree < 5-degree, $P = 0.024$; 30-degree < 10-degree, $P = 0.006$; and 30-degree < 20-degree, $P = 0.001$).

Target N2. Figure 4 shows the grand average waveforms (see Fig. 4a), topographic maps (see Fig. 4b), and the histograms of mean amplitudes (see Fig. 4c) for the target N2 component. There was a significant main effect of the defect condition (F (3, 117) = 34.953, $P < 0.001$, partial η^2

Table 1. Repeated-Measures ANOVA for the Amplitude of Target N2

Effect	dF	F	*P* Value	Partial η^2	Follow-up Tests
Defect (5, 10, 20, 30-degree)	3,117	34.953	0.000	0.473	5<20[a]; 5<30[c]; 10<20[b]; 10<30[c]; 20<30[c]
ROI (central-parietal, parietal)	1,39	0.293	0.591	0.007	
Laterality (left, middle, right)	2,78	4.750	0.011	0.109	left<right[a]
Defect × ROI	3,117	18.265	0.000	0.319	
Defect effect in central-parietal ROI	3,357	31.867	0.000	0.211	5<30[c]; 10<20[c]; 10<30[c]; 20<30[c]
Defect effect in parietal ROI	3,357	81.975	0.000	0.408	5<20[c]; 5<30[c]; 10<20[c]; 10<30[c]; 20<30[c]
ROI effect in 30-degree defect	1,119	39.613	0.000	0.250	central-parietal<parietal[c]
Defect × laterality	6,234	0.243	0.916	0.006	
Defect × ROI × laterality	6,234	1.609	0.169	0.040	

Defect condition indicates visual field defect.
ROI, regions of interest.
[a] $P < 0.05$.
[b] $P < 0.01$.
[c] $P < 0.001$.

Table 2. Repeated-Measures ANOVA for the Amplitude of Target P3

Effect	dF	F	*P* Value	Partial η^2	Follow-up Tests
Defect condition (5, 10, 20, 30-degree)	3,117	19.011	0.000	0.328	5>20[b]; 5>30[c]; 10>20[a]; 10>30[c]; 20>30[b]
ROI (central-parietal, parietal)	1,39	11.827	0.001	0.233	central-parietal<parietal[c]
Laterality (left, middle, right)	2,78	12.258	0.000	0.239	left>right[a]; middle>right[c]
Defect × ROI	3,117	8.169	0.000	0.173	
Defect effect in central-parietal ROI	3,357	22.785	0.000	0.161	5>20[c]; 5>30[c]; 10>20[c]; 10>30[c]; 20>30[b]
Defect effect in parietal ROI	3,357	45.247	0.000	0.275	5>20[c]; 5>30[c]; 10>20[c]; 10>30[c]; 20>30[c]
ROI effect in 5-degree defect	1,119	32.454	0.000	0.214	central-parietal<parietal[c]
ROI effect in 10-degree defect	1,119	18.489	0.000	0.134	central-parietal<parietal[c]
ROI effect in 20-degree defect	1,119	20.831	0.000	0.149	central-parietal<parietal[c]
Defect × laterality	6,234	2.483	0.024	0.060	
Defect effect in left hemisphere	3,237	40.236	0.000	0.337	5>20[c]; 5>30[c]; 10>20[a]; 10>30[c]; 20>30[c]
Defect effect in middle line	3,237	19.579	0.000	0.199	5>20[c]; 5>30[c]; 10>20[b]; 10>30[c]; 20>30[b]
Defect effect in right hemisphere	3,237	13.289	0.000	0.144	5>20[c]; 5>30[c]; 10>20[b]; 10>30[c]
Laterality effect in 5-degree defect	2,158	11.890	0.000	0.131	left>right[b]; middle>right[c]
Laterality effect in 10-degree defect	2,158	15.017	0.000	0.160	left>right[b]; middle>right[c]
Laterality effect in 20-degree defect	2,158	15.867	0.000	0.167	left>right[c]; middle>right[c]
Laterality effect in 30-degree defect	2,158	6.645	0.003	0.078	left>middle[c]; middle>right[a]
Defect × ROI × laterality	6,234	0.858	0.481	0.022	

Defect condition indicates visual field defect.
ROI, regions of interest.
[a] $P < 0.05$.
[b] $P < 0.01$.
[c] $P < 0.001$.

= 0.473) and laterality (F (2, 78) = 4.750, $P = 0.011$, partial $\eta^2 = 0.109$). There was a significant interaction of the defect condition and ROI (F (3, 117) = 18.265, $P < 0.001$, partial $\eta^2 = 0.319$). Detailed main effects and interaction effects of the target N2 amplitude are shown in Table 1.

Target P3. Figure 4 shows the grand average waveforms (see Fig. 4a), topographic maps (see Fig. 4d), and the histograms of mean amplitudes (see Fig. 4e) for the target P3 component. There was a significant main effect of the defect condition (F (3, 117) = 19.011, $P < 0.001$, partial $\eta^2 = 0.328$), ROI (F (1, 39) = 11.827, $P = 0.001$, partial $\eta^2 = 0.233$), and laterality (F (2, 78) = 12.258, $P < 0.001$, partial $\eta^2 = 0.239$). There was also a significant interaction of the defect condition and ROI (F (3, 117) = 8.169, $P < 0.001$, partial $\eta^2 = 0.173$) and the defect condition and laterality (F (6, 234) = 2.483, $P = 0.024$, partial $\eta^2 = 0.060$). Detailed main effects and interaction effects of the target P3 amplitude are shown in Table 2.

For target P3 peak latency, there was a significant main effect of the defect condition (F (3, 117) = 11.669, $P < 0.001$, partial $\eta^2 = 0.230$) and ROI (F (1, 39) = 11.467, $P = 0.002$, partial $\eta^2 = 0.227$). There was a significant interaction of the defect condition and ROI (F (3, 117) = 4.430, $P = 0.005$, partial $\eta^2 = 0.102$). Detailed main effects and interaction effects of the target P3 latency are shown in Table 3.

sLORETA Results

Significant differences in the standardized current density between visual field defect conditions were only found for target P2, N2, and P3 components. Therefore, further analysis was shown based on target P2, N2, and P3 components.

Target P2 Source Activations. Figure 5 shows the grand average source images (see Fig. 5a) and the histograms of averaged source activations (see Fig. 5b) for the target P2 component. There was a significant main effect of the defect condition in the right ventrolateral prefrontal regions (BA 11, 45, and 47; F (3, 117) = 5.320, $P = 0.002$, partial $\eta^2 = 0.120$), indicating that the source activity of 5-degree, 10-degree, and 20-degree defects were smaller than

Investigative Ophthalmology & Visual Science

Table 3. Repeated-Measures ANOVA for the Peak Latency of Target P3

Effect	dF	F	*P* Value	Partial η^2	Follow-up Tests
Defect condition (5, 10, 20, 30-degree)	3,117	11.669	0.000	0.230	5<30[c]; 10<30[c]; 20<30[c]
ROI (central-parietal, parietal)	1,39	11.467	0.002	0.227	central-parietal>parietal[b]
Laterality (left, middle, right)	2,78	0.481	0.583	0.012	
Defect × ROI	3,117	4.430	0.005	0.102	
Defect effect in central-parietal ROI	3,357	14.330	0.000	0.107	10<20[a]; 5<30[c]; 10<30[c]; 20<30[b]
Defect effect in parietal ROI	3,357	17.847	0.000	0.130	5<30[c]; 10<30[c]; 20<30[c]
ROI effect in 5-degree defect	1,119	5.718	0.018	0.046	central-parietal>parietal[b]
ROI effect in 30-degree defect	1,119	24.139	0.000	0.169	central-parietal>parietal[c]
Defect × laterality	6,234	1.287	0.275	0.032	
Defect × ROI × laterality	6,234	0.769	0.595	0.019	

Defect condition indicates visual field defect.
ROI, regions of interest.
[a] $P < 0.05$.
[b] $P < 0.01$.
[c] $P < 0.001$.

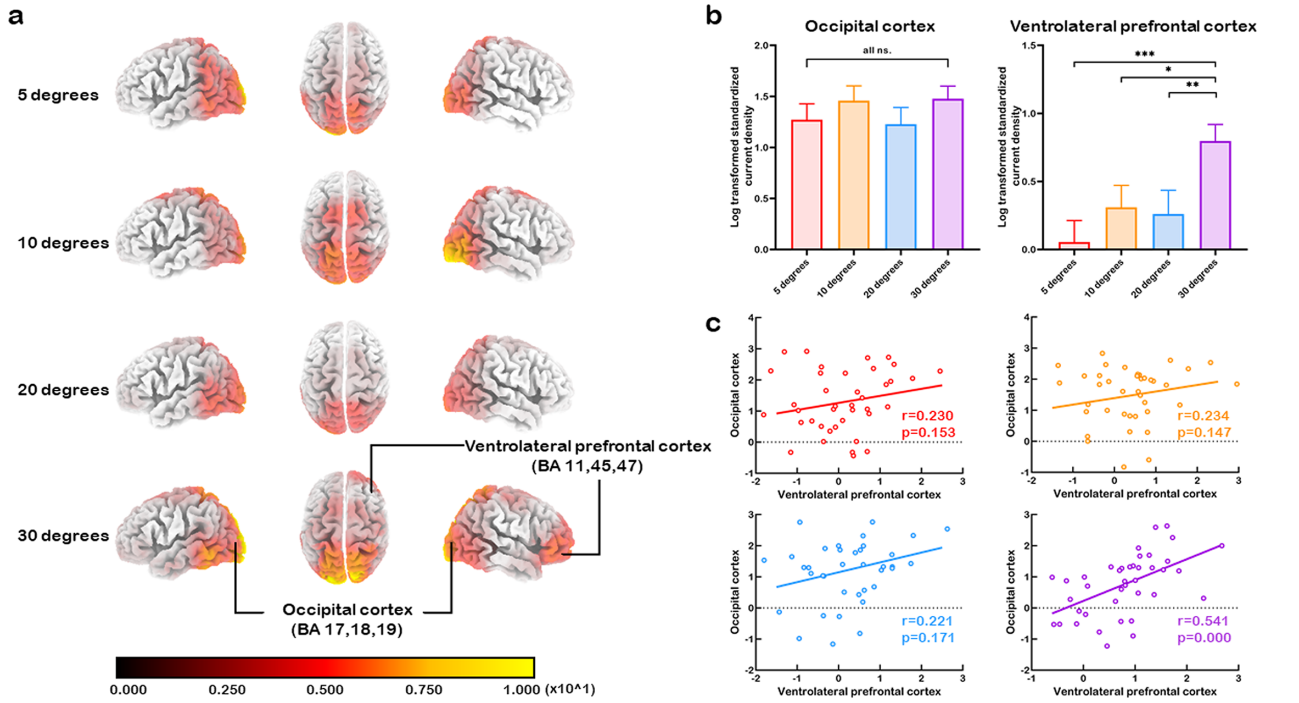

Figure 5. Source localization results for the target P2 component. (**a**) Grand average source images within the target P2 time window (approximately 170 to 230 ms). The first row to the fourth row represents the 5, 10, 20, and 30-degree defect conditions, respectively. *Red* and *yellow* colors indicate significantly higher activations. (**b**) Statistical results of significant activations in the P2 time window (log-transformed standardized current density in μV/mm^2 units) for each defect condition (*red*, *orange*, *blue*, and *purple bars* indicate the 5, 10, 20, and 30-degree defect conditions, respectively). (**c**) Correlation results between significant source activations for the target P2 component, illustrating the least-squares regression line and associated Pearson correlation coefficients (*red*, *orange*, blue, and *purple* indicate the 5, 10, 20, and 30-degree defect conditions, respectively).

that of 30-degree defects (5-degree < 30-degree, $P = 0.001$; 10-degree < 30-degree, $P = 0.015$; and 20-degree < 30-degree, $P = 0.007$).

Target N2 Source Activations. Figure 6 shows the grand average source images (see Fig. 6a) and the histograms of averaged source activations (see Fig. 6b) for the target N2 component. There was a significant main effect of the defect condition in the right occipital regions (BA 17, 18, and 19; F (3, 117) = 4.364, $P = 0.006$, partial $\eta^2 = 0.101$), indicating that the source activity of 5-degree, 10-degree, and 20-degree defects were smaller than that of 30-degree defects (5-degree < 30-degree, $P = 0.001$; 10-degree < 30-degree, $P = 0.023$; and 20-degree < 30-degree, $P = 0.001$). There was a significant main effect of the defect condition in the right inferior temporal regions (BA 20, 21, 22, and 38; F (3, 117) = 6.238, $P = 0.001$, partial $\eta^2 = 0.138$), indicating that the source activity of 5-degree, 10-degree, and 20-degree defects was smaller than that of 30-degree defects (5-degree < 30-degree, $P = 0.002$; 10-degree < 30-degree, $P = 0.003$; and 20-degree < 30-degree, $P < 0.001$). There was a significant main effect of the defect condition in the right ventrolateral prefrontal regions (BA 11, 45, and 47; F (3, 117)

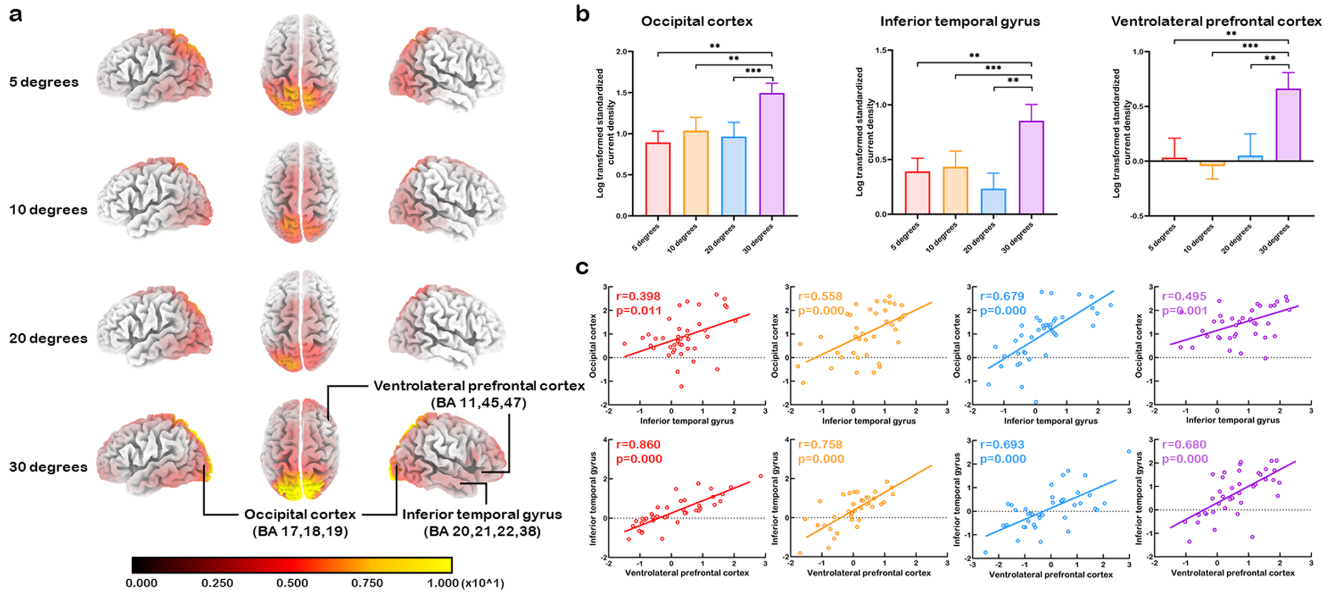

Figure 6. Source localization results for the target N2 component. (**a**) Grand average source images within the target N2 time window (approximately 230 to 270 ms). The first row to the fourth row represents the 5, 10, 20, and 30-degree defect conditions, respectively. The *red* and *yellow* colors indicate significantly higher activations. (**b**) Statistical results of significant activations in the N2 time window (log-transformed standardized current density in μV/mm^2 units) for each defect condition (*red*, *orange*, *blue*, and *purple bars* indicate the 5, 10, 20, and 30-degree defect conditions, respectively). (**c**) Correlation results between significant source activations for the target N2 component, illustrating the least-squares regression line and associated Pearson correlation coefficients (*red*, *orange*, *blue*, and *purple* indicate the 5, 10, 20, and 30-degree defect conditions, respectively).

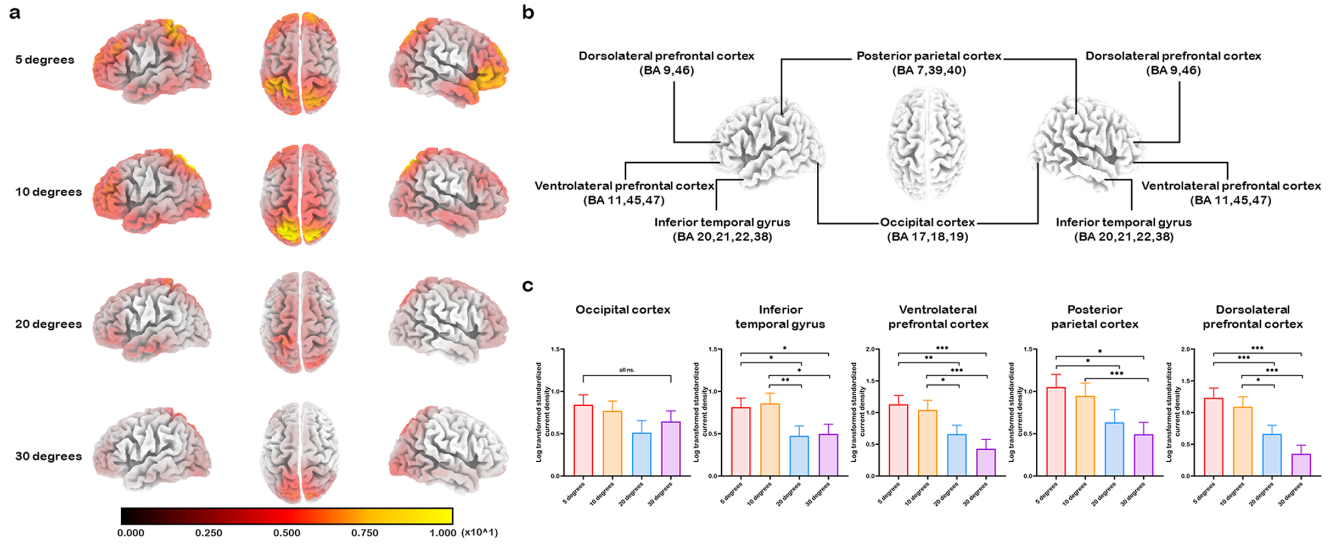

Figure 7. Source localization results for the target P3 component. (**a**) Grand average source images within the target P3 time window (approximately 300 to 500 ms). The first row to the fourth row represents the 5, 10, 20, and 30-degree defect conditions, respectively. The *red* and *yellow* colors indicated significantly higher activations. (**b**) Graphical representation of the significant source activations in the P3 time window illustrated by Broadman areas. (**c**) Statistical results of significant activations in the P3 time window (log-transformed standardized current density in μV/mm^2 units) for each defect condition (*red*, *orange*, *blue*, and *purple bars* indicate the 5, 10, 20, and 30-degree defect conditions, respectively).

= 6.002, $P = 0.001$, partial $\eta^2 = 0.133$), indicating that the source activity of 5-degree, 10-degree, and 20-degree defects was smaller than that of 30-degree defects (5-degree < 30-degree, $P = 0.004$; 10-degree < 30-degree, $P < 0.001$; and 20-degree < 30-degree, $P = 0.002$).

Target P3 Source Activations. Figure 7 shows the grand average source images (see Fig. 7a), illustration of the main activated brain regions (see Fig. 7b), and the histograms of averaged source activations (see Fig. 7c) for the target P3 component. There was a significant main effect of the defect condition ($F(3, 117) = 11.222$, $P < 0.001$, partial $\eta^2 = 0.223$) in the dorsolateral prefrontal regions (BA 9 and 46), indicating that the source activity of 5-degree and 10-degree defects was larger than that of 20-degree and 30-

degree defects (5-degree > 20-degree, $P = 0.001$; 5-degree > 30-degree, $P < 0.001$; 10-degree > 20-degree, $P = 0.012$; and 10-degree > 30-degree, $P < 0.001$). There was also a significant main effect of the defect condition (F (3, 117) = 4. 826, $P = 0.003$, partial $\eta^2 = 0.110$) in the posterior parietal regions (BA 7, 39, and 40), indicating that the source activity of 5-degree and 10-degree defects was larger than that of 20-degree and 30-degree defects (5-degree > 20-degree, $P = 0.011$; 5-degree > 30-degree, $P = 0.001$; and 10-degree > 30-degree, $P = 0.018$).

There was a significant main effect of the defect condition (F (3, 117) = 7.266, $P < 0.001$, partial $\eta^2 = 0.157$) in the ventrolateral prefrontal regions (BA 11, 45, and 47), indicating that the source activity of 5-degree and 10-degree defects was larger than that of 20-degree and 30-degree defects (5-degree > 20-degree, $P = 0.005$; 5-degree > 30-degree, $P < 0.001$; 10-degree > 20-degree, $P = 0.024$; and 10-degree > 30-degree, $P = 0.001$). There was also a significant main effect of the defect condition (F (3, 117) = 4.088, $P = 0.008$, partial $\eta^2 = 0.095$) in the inferior temporal regions (BA 20, 21, 22, and 38), indicating that the source activity of 5-degree and 10-degree defects were larger than that of 20-degree and 30-degree defects (5-degree > 20-degree, $P = 0.013$; 5-degree > 30-degree, $P = 0.027$; 10-degree > 20-degree, $P = 0.003$; and 10-degree > 30-degree, $P = 0.017$).

Correlation Results

For correlation analysis, Pearson's correlation coefficients (r and P values) are listed in Supplementary Table S2.

For P2 source activations, right ventrolateral prefrontal activations were positively correlated with right occipital activations only under 30-degree defect conditions (see Fig. 5c).

For N2 source activations, right occipital activations were positively correlated with right inferior temporal activations among all defect conditions, whereas right inferior temporal activations were positively correlated with right ventrolateral prefrontal activations among all defect conditions (see Fig. 6c).

For P3 source activations, bilateral occipital activations were positively correlated with bilateral posterior parietal activations among all defect conditions, whereas bilateral posterior parietal activations were positively correlated with bilateral dorsolateral prefrontal activations only under the 5-degree, 10-degree, and 20-degree defect conditions. Bilateral occipital activations were positively correlated with bilateral inferior temporal activations among all defect conditions, whereas bilateral inferior temporal activations were positively correlated with bilateral ventrolateral prefrontal activations among all defect conditions (see Supplementary Fig. S1).

Discussion

By using ERP and sLORETA methods, we investigated spatiotemporal dynamics of attentional deployment when simulating central visual field defects. There were several stages of attentional processing when simulating visual field defects.[46,47] First, information inputs under simulated defect conditions captured attention through initial perceptual processing (indexed by N1) to form preliminary representations in the occipital cortex. Second, the higher prefrontal cortex evaluated visual representations and gave forward feedback to the occipital cortex to reactivate visual representations (indexed by P2). Subsequently, the ventral occipital-temporal-prefrontal cortices modulated the comparison between visual representation inputs and internal memory representations (indexed by N2). Finally, the dorsal occipital-parietal-prefrontal cortices allocated attentional resources and made final decisions (indexed by P3).

Visual N1 is considered the earliest indicator of visual attention and appears to be pronounced when subjects perform a discrimination task.[48] In our study, N1 amplitudes over the posterior scalp regions significantly distinguished 5-degree and 10-degree defects from 20-degree and 30-degree defects, indicating that visual N1 is more informative for target discrimination and discriminates one type of stimulus from another in the attended visual field. According to the capacity theory,[49,50] perceptual load modulates voluntary attentional effects on posterior N1. Thus, N1 modulations showed a load effect sensitive to stimulus location in the attended visual field, indicating that higher load defects had more negative amplitudes. Source analysis indicated that visual N1 activated a larger area of temporal-parietal-occipital cortices, consistent with recent functional magnetic resonance imaging (fMRI) evidence suggesting that the temporoparietal junction is critical for target discrimination.[51] However, the source activations of N1 did not differ between defect conditions. One possible explanation was that artificial deprivation of information inputs in the central visual field generated transient sensory deprivation in the primary visual cortex and caused no difference in the bottom-up visual processing based on low-level stimulus features.

P2 reflects higher-order perceptual processes and is sensitive to spatial locations in the visual field.[52] The 30-degree defects elicited a much smaller P2 amplitude than other defects, implying dysfunction of perceptual processes. Source analysis of P2 indicated widespread activations in the occipital cortex. The 30-degree defects also activated the right ventrolateral prefrontal cortex, and there was a strong correlation between the ventrolateral prefrontal cortex and occipital cortex. Evidence suggested that P2 might be associated with reactivation of the occipital cortex, due to top-down re-entrant feedback from higher-level visual areas back to the early visual cortex.[53,54] Consistent with these studies, our study further suggested that 30-degree defects recruited a top-down modulation to re-activate the residual information inputs to enhance visual representations. Thus, visual attention might enhance visual representations via top-down feedback mechanisms, especially in high-level defects with limited visual inputs.

After perceptual processing, the incoming representations underwent subsequent cognitive processing with the internal representations in memory. N2 is responsible for stimulus classification and conflict monitoring, reflecting cognitive matching processes with stored memory.[55] The observed N2 had a predominantly parietal scalp distribution, which is consistent with previous studies indicating that posterior N2 may be specific to the visual modality.[56] It has been also suggested that posterior N2 amplitude is directly correlated with the difficulty of recognition and discrimination.[57] In this study, N2 amplitudes increased as simulated defects increased and were further categorized into three groups: 5-degree and 10-degree defects, 20-degree defects, and 30-degree defects. These results were consistent with the typical categorization of the central visual field, that is foveal, parafoveal, and perifoveal visual fields.[58,59] As

Investigative Ophthalmology & Visual Science

central defects enlarged, the difficulty in capturing peripheral visual stimulation increased, and more top-down attentional resources were needed for distinguishing between visual representation inputs and stored memory representations. Thus, low-level defects of 5-degree and 10-degree can be better identified and compared with internal memory representation, whereas high-level defects of 20-degree and 30-degree adjusted their attentional modulation according to the demands caused by increased difficulty, resulting in a generally increased N2 amplitude.

Source localization of N2 indicated that the occipital cortex, inferior temporal gyrus, and ventrolateral prefrontal cortex were predominantly involved in the differentiation of defect conditions. Occipital-temporal-prefrontal activations were located in the ventral stream for visual processing, reflecting more specific attentional processing based on object information, characterized as the "What" pathway.[60] Our findings revealed that the 30-degree defects suffered the worst information inputs and recruited the strongest activation in the right-lateralized ventral stream to compensate for central visual field dysfunction. These results suggested that visual processing identified visual field defect conditions through a ventral stream specialized for object recognition.

Finally, pronounced P3 components were induced over the central-parietal scalp regions. P3 amplitude is determined by the allocation of attentional resources, whereas P3 latency represents the processing speed of stimuli evaluation and classification.[61] In this study, P3 amplitudes decreased as the central defects enlarged, which distinguished 5-degree and 10-degree defects from 20-degree and 30-degree defects. These results indicated that P3 amplitudes varied with the amount of allocated attentional resources according to the spatial distribution of the attended visual field. P3 latency was delayed in 30-degree defects than in other defect conditions, which spent more time evaluating and classifying stimuli in the same discrimination task.

Source localization of P3 indicated that the bilateral occipital cortex, inferior temporal gyrus, ventrolateral prefrontal cortex, posterior parietal cortex, and dorsolateral prefrontal cortex were jointly engaged in the differentiation of defect conditions. For one thing, 5-degree and 10-degree defects had stronger activations than 20-degree and 30-degree defects in these cortices. The fact that neural responses to visual stimulations were selectively enhanced in low-level defects rather than in high-level defects might be caused by qualitative differences in neural processing between the central and peripheral visual fields.[62,63] For another, different source activations were interconnected to form the ventral stream and the dorsal stream. Our findings supported the "two visual systems" hypothesis for visual processing, which functionally segregates brain responses into two relatively independent streams.[64,65] Compared with 20-degree and 30-degree defects, 5-degree and 10-degree defects had better object recognition through ventral activations and better response execution through dorsal activations. Nevertheless, 30-degree defects seriously impaired the correlation between the dorsolateral frontal cortex and posterior parietal cortex. Considering that the dorsolateral prefrontal cortex serves as top-down executive control and the posterior parietal cortex facilitates sensorimotor executions,[66] 30-degree defects resulted in poor executive performance due to disrupted visually guided behavior. In summary, bilateral ventral and dorsal streams collectively differentiated defect degrees of the central visual field.

Despite significance in our findings, there are limitations to this study. First, manipulation of target size may involve many additional factors like signal-to-noise ratio (SNR), center-surround inhibitions of neural activities, and object-background segregation. Therefore, instructing participants on stable fixation and good cooperation online to eliminate object-background segregation, and conducting strict data inclusion criteria offline to counterbalance external factors, such as SNR and center-surround inhibitions, among individuals were approaches to ensure the validity of EEG data. Comparative analysis based on different target stimuli each can further reduce the variance among individuals and make the significant results dominated by the specific stimulus itself to eliminate the influence of stimulus pattern to a larger extent. Second, normal participants were able to visualize simulated scotoma, whereas patients with pathologically generated central visual field defects are unaware of scotoma due to perceptual "filling-in" and are often accompanied by additional symptoms. To verify and expand the current findings in the future study, we may enroll the experimental subjects and assess the effect of duration of vision loss on cortical function, and further include clinical patients with different types of visual field defects such as macular degeneration, degenerative myopia, and other related ophthalmological diseases, as experimental controls. Third, our source localization findings based on 32-channel configurations can be considered as an exploratory investigation and should be interpreted with caution due to the relative limits of spatial resolution and potential localization, which needs to be further testified with high-density EEG and high-resolution techniques to more accurately estimate activity in the brain regions.

In conclusion, combined ERPs with source localization analysis, we revealed characteristics of different degrees of simulated central visual field defects through distinct spatiotemporal measures of covert attention. First, bottom-up processing made no difference for simulated visual field defects, suggesting that coarse sensory-perceptual processes based on low-level stimulus characteristics were not affected. Second, due to the increasing discrimination difficulty from 5-degree defects to 30-degree defects, top-down processing significantly classified simulated defects into 3 groups. The 5-degree and 10-degree defects resulted in less disruption of the primary visual input, and the vision system is better at integrating information and performing executive controls. The 30-degree occlusion resulted in compensation for the loss of visual inputs and the decrease in discrimination was likely due to forward feedback and attentional control. Nevertheless, the 30-degree defects failed to integrate all forms of information based on the disrupted visually guided behavior. The 20-degree defects resulted in the adjustment of the strength of cortical processing to accommodate moderate defects. These findings reconfirmed the functional hierarchy of the central visual field through different cortices involved and the strength of cortical processing and allowed visualization of specific visual processing streams to modulate simulated central visual field defects.

Acknowledgments

Supported by the National Natural Science Foundation of China (No. 81871536 and 81971800). The authors also appreciate the support from the Priority Academic Program Development of Jiangsu Higher Education Institutes (PAPD), China.

Investigative Ophthalmology & Visual Science

Author Contributions: T.L. and C.X. conceived and designed this research. S.C. and L.S. performed experiments. Z.B., M.Y., and G.X. engaged in data analysis. S.C., L.S., T.L., and C.X. wrote the manuscript article. All authors have read and agreed to the published version of the manuscript.

Disclosure: **C. Shi**, None; **S. Liu**, None; **B. Zhao**, None; **Y. Meng**, None; **X. Gong**, None; **X. Chen**, None; **L. Tao**, None

References

1. Carrasco M. Visual attention: the past 25 years. *Vision Res*. 2011;51:1484–1525.
2. Fernandez A, Okun S, Carrasco M. Differential Effects of Endogenous and Exogenous Attention on Sensory Tuning. *J Neurosci*. 2022;42:1316–1327.
3. Karim AK, Kojima H. The what and why of perceptual asymmetries in the visual domain. *Adv Cogn Psychol*. 2010;6:103–115.
4. Weiss K. Exogeneous Spatial Cueing beyond the Near Periphery: Cueing Effects in a Discrimination Paradigm at Large Eccentricities. *Vision (Basel)*. 2020;4:13.
5. Bao Y, Wang Y, Poppel E. Spatial orienting in the visual field: a unified perceptual space? *Cogn Process*. 2012;13(Suppl 1):S93–S96.
6. Bao Y, Poppel E. Two spatially separated attention systems in the visual field: evidence from inhibition of return. *Cogn Process*. 2007;8:37–44.
7. Handy TC, Khoe W. Attention and sensory gain control: a peripheral visual process? *J Cogn Neurosci*. 2005;17:1936–1949.
8. Yang T, Zhang J, Bao Y. Spatial orienting around the fovea: exogenous and endogenous cueing effects. *Cogn Process*. 2015;16(Suppl 1):137–141.
9. Di Russo F, Martinez A, Sereno MI, Pitzalis S, Hillyard SA. Cortical sources of the early components of the visual evoked potential. *Hum Brain Mapp*. 2002;15:95–111.
10. Bertera JH. The effect of simulated scotomas on visual search in normal subjects. *Invest Ophthalmol Vis Sci*. 1988;29:470–475.
11. McIlreavy L, Fiser J, Bex PJ. Impact of simulated central scotomas on visual search in natural scenes. *Optom Vis Sci*. 2012;89:1385–1394.
12. Hummer A, Ritter M, Woletz M, et al. Artificial scotoma estimation based on population receptive field mapping. *Neuroimage*. 2018;169:342–351.
13. Yadav NK, Ludlam DP, Ciuffreda KJ. Effect of different stimulus configurations on the visual evoked potential (VEP). *Doc Ophthalmol*. 2012;124:177–196.
14. Gannon MA, Long SM, Parks NA. Homeostatic plasticity in human extrastriate cortex following a simulated peripheral scotoma. *Exp Brain Res*. 2017;235:3391–3401.
15. Odom JV, Bach M, Brigell M, et al. ISCEV standard for clinical visual evoked potentials: (2016 update). *Doc Ophthalmol*. 2016;133:1–9.
16. Hillyard SA, Vogel EK, Luck SJ. Sensory gain control (amplification) as a mechanism of selective attention: electrophysiological and neuroimaging evidence. *Philos Trans R Soc Lond B Biol Sci*. 1998;353:1257–1270.
17. Vogel EK, Luck SJ. The visual N1 component as an index of a discrimination process. *Psychophysiology*. 2000;37:190–203.
18. Desjardins M, Drisdelle BL, Lefebvre C, Gagnon JF, De Beaumont L, Jolicoeur P. Interhemispheric differences in P1 and N1 amplitude in EEG and MEG differ across older individuals with a concussion compared with age-matched controls. *Psychophysiology*. 2021;58:e13751.
19. Capilla A, Melcon M, Kessel D, Calderon R, Pazo-Alvarez P, Carretie L. Retinotopic mapping of visual event-related potentials. *Biol Psychol*. 2016;118:114–125.
20. Warren CM, Tanaka JW, Holroyd CB. What can topology changes in the oddball N2 reveal about underlying processes? *Neuroreport*. 2011;22:870–874.
21. Huang WJ, Chen WW, Zhang X. The neurophysiology of P 300–an integrated review. *Eur Rev Med Pharmacol Sci*. 2015;19:1480–1488.
22. Pascual-Marqui RD. Standardized low-resolution brain electromagnetic tomography (sLORETA): technical details. *Methods Find Exp Clin Pharmacol*. 2002;24(Suppl D):5–12.
23. Di Russo F, Martinez A, Sereno MI, Pitzalis S, Hillyard SA. Cortical sources of the early components of the visual evoked potential. *Hum Brain Mapp*. 2002;15:95–111.
24. Martínez A, Anllo-Vento L, Sereno MI, Frank LR, Hillyard SA. Involvement of striate and visual cortical areas in spatial attention. *Nat Neurosci*. 1999;2:364–369.
25. Milner AD, Goodale MA. Two visual systems re-viewed. *Neuropsychologia*. 2008;46:774–785.
26. Squire RF, Noudoost B, Schafer RJ, Moore T. Prefrontal contributions to visual selective attention. *Annu Rev Neurosci*. 2013;36:451–466.
27. Shigihara Y, Hoshi H, Zeki S. Early visual cortical responses produced by checkerboard pattern stimulation. *Neuroimage*. 2016;134:532–539.
28. Polich J. Updating P300: an integrative theory of P3a and P3b. *Clin Neurophysiol*. 2007;118:2128–2148.
29. Delorme A, Makeig S. EEGLAB: an open source toolbox for analysis of single-trial EEG dynamics including independent component analysis. *J Neurosci Methods*. 2004;134:9–21.
30. Delorme A, Sejnowski T, Makeig S. Enhanced detection of artifacts in EEG data using higher-order statistics and independent component analysis. *Neuroimage*. 2007;34:1443–1449.
31. Kappenman ES, Luck SJ. *The Oxford Handbook of Event-Related Potential Components*; 2011. Luck S, Kappenman ES , eds. New York, NY: Oxford University Press; 2011.
32. Luck SJ. *An introduction to the event-related potential technique*. Cambridge, MA: MIT Press; 2005:374.
33. Luck SJ, Gaspelin N. How to get statistically significant effects in any ERP experiment (and why you shouldn't). *Psychophysiology*. 2017;54:146–157.
34. Pascual-Marqui RD. Standardized low-resolution brain electromagnetic tomography (sLORETA): technical details. *Methods Find Exp Clin Pharmacol*. 2002;24(Suppl D):5–12.
35. Fuchs M, Kastner J, Wagner M, Hawes S, Ebersole JS. A standardized boundary element method volume conductor model. *Clin Neurophysiol*. 2002;113:702–712.
36. Mazziotta J, Toga A, Evans A, et al. A four-dimensional probabilistic atlas of the human brain. *J Am Med Inform Assoc*. 2001;8:401–430.
37. Song J, Davey C, Poulsen C, et al. EEG source localization: Sensor density and head surface coverage. *J Neurosci Methods*. 2015;256:9–21.
38. Albert J, Lopez-Martin S, Tapia M, Montoya D, Carretie L. The role of the anterior cingulate cortex in emotional response inhibition. *Hum Brain Mapp*. 2012;33:2147–2160.
39. Mulert C, Jager L, Schmitt R, et al. Integration of fMRI and simultaneous EEG: towards a comprehensive understanding of localization and time-course of brain activity in target detection. *Neuroimage*. 2004;22:83–94.
40. Hong X, Sun J, Wang J, Li C, Tong S. Attention-related modulation of frontal midline theta oscillations in cingulate cortex during a spatial cueing Go/NoGo task. *Int J Psychophysiol*. 2020;148:1–12.
41. Hong X, Wang Y, Sun J, Li C, Tong S. Segregating Top-Down Selective Attention from Response Inhibition in a Spatial

Investigative Ophthalmology & Visual Science

Cueing Go/NoGo Task: An ERP and Source Localization Study. *Sci Rep*. 2017;7:9662.
42. Chica AB, Bartolomeo P, Lupianez J. Two cognitive and neural systems for endogenous and exogenous spatial attention. *Behav Brain Res*. 2013;237:107–123.
43. Ludwig K, Sterzer P, Kathmann N, Hesselmann G. Differential modulation of visual object processing in dorsal and ventral stream by stimulus visibility. *Cortex*. 2016;83:113–123.
44. Faul F, Erdfelder E, Lang AG, Buchner A. G*Power 3: a flexible statistical power analysis program for the social, behavioral, and biomedical sciences. *Behav Res Methods*. 2007;39:175–191.
45. Cohen J. *The Statistical Power Analysis for the Behavioral Sciences 2nd Ed*. New York, NY: Routledge Publishing; 1988.
46. Franz M, Schmidt B, Hecht H, Naumann E, Miltner W. Suggested visual blockade during hypnosis: Top-down modulation of stimulus processing in a visual oddball task. *PLoS One*. 2021;16:e257380.
47. Kasai T, Takeya R, Tanaka S. Emergence of visual objects involves multiple stages of spatial selection. *Atten Percept Psychophys*. 2015;77:441–449.
48. Luo YJ, Greenwood PM, Parasuraman R. Dynamics of the spatial scale of visual attention revealed by brain event-related potentials. *Brain Res Cogn Brain Res*. 2001;12:371–381.
49. Handy TC, Mangun GR. Attention and spatial selection: electrophysiological evidence for modulation by perceptual load. *Percept Psychophys*. 2000;62:175–186.
50. Tan J, Zhao Y, Wang L, et al. The Competitive Influences of Perceptual Load and Working Memory Guidance on Selective Attention. *PLoS One*. 2015;10:e129533.
51. Hopf JM, Vogel E, Woodman G, Heinze HJ, Luck SJ. Localizing visual discrimination processes in time and space. *J Neurophysiol*. 2002;88:2088–2095.
52. Omoto S, Kuroiwa Y, Otsuka S, et al. P1 and P2 components of human visual evoked potentials are modulated by depth perception of 3-dimensional images. *Clin Neurophysiol*. 2010;121:386–391.
53. Di Russo F, Aprile T, Spitoni G, Spinelli D. Impaired visual processing of contralesional stimuli in neglect patients: a visual-evoked potential study. *Brain*. 2008;131:842–854.
54. Zhong H, Zhao S, Chen T, Yang W, Huang X, Feng W. Temporal dynamics of the flash-induced bouncing effect. *Hum Brain Mapp*. 2020;41:3009–3018.
55. Bocquillon P, Bourriez JL, Palmero-Soler E, Molaee-Ardekani B, Derambure P, Dujardin K. The spatiotemporal dynamics of early attention processes: a high-resolution electroencephalographic study of N2 subcomponent sources. *Neuroscience*. 2014;271:9–22.
56. Folstein JR, Van Petten C. Influence of cognitive control and mismatch on the N2 component of the ERP: a review. *Psychophysiology*. 2008;45:152–170.
57. Senkowski D, Herrmann CS. Effects of task difficulty on evoked gamma activity and ERPs in a visual discrimination task. *Clin Neurophysiol*. 2002;113:1742–1753.
58. Bringmann A, Syrbe S, Gorner K, et al. The primate fovea: Structure, function and development. *Prog Retin Eye Res*. 2018;66:49–84.
59. Yazdani N, Ehsaei A, Hoseini-Yazdi H, Shoeibi N, Alonso-Caneiro D, Collins MJ. Wide-field choroidal thickness and vascularity index in myopes and emmetropes. *Ophthalmic Physiol Opt*. 2021;41:1308–1319.
60. Kravitz DJ, Saleem KS, Baker CI, Ungerleider LG, Mishkin M. The ventral visual pathway: an expanded neural framework for the processing of object quality. *Trends Cogn Sci*. 2013;17:26–49.
61. Kok A. On the utility of P3 amplitude as a measure of processing capacity. *Psychophysiology*. 2001;38:557–577.
62. Kupers ER, Carrasco M, Winawer J. Modeling visual performance differences 'around' the visual field: A computational observer approach. *PLOS Comput Biol*. 2019;15:e1007063.
63. Poppel E, Bao Y. The visual field paradox: a theoretical account on the reafference principle providing a common frame for the homogeneity and inhomogeneity of visual representation. *Cogn Process*. 2012;13(Suppl 1):S285–S287.
64. Vossel S, Geng JJ, Fink GR. Dorsal and ventral attention systems: distinct neural circuits but collaborative roles. *Neuroscientist*. 2014;20:150–159.
65. Suo X, Ding H, Li X, et al. Anatomical and functional coupling between the dorsal and ventral attention networks. *Neuroimage*. 2021;232:117868.
66. Andersen RA, Cui H. Intention, action planning, and decision making in parietal-frontal circuits. *Neuron*. 2009;63:568–583.